Electrocatalysis (2020) 11:522–535
https://doi.org/10.1007/s12678-020-00611-0

ORIGINAL RESEARCH

Fabrication of Composite Material with Pd Nanoparticles and Graphene on Nickel Foam for Its Excellent Electrocatalytic Performance

Yanmei Shen[1] · Shixiang Lu[1] · Wenguo Xu[1] · Anqi Lv[1] · Ziwen Wang[1] · Hongtao Wang[1] · Guoxiao Liu[1] · Yan Zhang[2]

Published online: 14 June 2020

Abstract

Incorporation of precious metallic nanoparticles onto a carbon support material is used to obtain an electrocatalyst for ethanol oxidation. A composite material of spherical palladium nanoparticles (Pd NPs), reduced graphene oxide (rGO), and polydopamine (PDA) on three-dimensional nickel foam (NF) substrate (Pd/rGO/PDA@NF) has been synthesized for ethanol electrocatalysis. The Pd nanoparticles were obtained via reduction of precursor K_2PdCl_4 using ascorbic acid at 60 °C for 80 min. The rGO with large specific surface area was used in catalysts to provide large amounts of active sites for Pd NPs. Meanwhile, Pd NPs as an effective ingredient in catalyst exhibited excellent electrochemical activity of ethanol oxidation. Local surface plasmon resonance was carried out to determine the optimal concentration of precursor K_2PdCl_4 aqueous solution, and the absorbance peak of Pd NPs was found at about 340–370 nm by UV-visible spectroscopy. An enhanced property of the composite material Pd/rGO/PDA@NF was demonstrated to catalyze the ethanol oxidation reaction in alkaline electrolyte solution. A higher ratio of forward scan peak current intensity (I_f) to reverse scan peak current intensity (I_b) was 1.59, which demonstrated the significant anti-poison effect to carbonaceous intermediates of the Pd/rGO/PDA@NF. The value of I_f can maintain 90.6% after 400 cycles, indicating the higher cycling stability and better electrocatalytic performance toward ethanol oxidation.

Keywords Pd nanoparticles · Ethanol electrocatalysis · Graphene · Polydopamine · Nickel foam

Introduction

Nowadays, direct ethanol fuel cells (DEFCs) have received great attention owing to the higher energy density and less environmental pollution than traditional fossil fuels [1]. Ethanol, as the hydrogen-rich and non-toxic liquid in DEFCs, exhibits more advantages, such as low toxicity and environmental compatibility [2]. Therefore, DEFCs have become clean and high energy sources for sustainable fuel, in which the effective ethanol electro-oxidation reaction is one of the major factors affecting cells property [3].

A great electrocatalyst in ethanol electrochemical oxidation reaction of DEFCs can provide excellent electrocatalytic performance for high energy conversion efficiency and low toxicity [4]. Accordingly, the noble metallic materials have been synthesized to be used as efficient ingredients in electrocatalyst for ethanol oxidation reaction (EOR). The palladium (Pd)-based electrocatalysts will promise to become the substitute of platinum (Pt)-based catalysts because Pd can improve the activity, stability, and good tolerance against carbon intermediate species during EOR process [5, 6]. Meanwhile, Pd-based electrocatalyst has demonstrated the better ability to break C-C bond of ethanol in alkaline media as compared with Pt-based catalyst [7]. Moreover, the high cost and limited supply of Pt compose the major obstacle to the development of electrocatalyst for fuel cells [8]. The abundance of Pd on the Earth's crust is 200 times more than Pt, and the relatively low price of Pd makes it suitable for broad-scale fuel cell

Electronic supplementary material The online version of this article (https://doi.org/10.1007/s12678-020-00611-0) contains supplementary material, which is available to authorized users.

✉ Shixiang Lu
shixianglu@bit.edu.cn

✉ Wenguo Xu
xuwg60@bit.edu.cn

[1] School of Chemistry and Chemical Engineering, Beijing Institute of Technology, Beijing 100081, People's Republic of China

[2] State Grid Corp of China Shandong Electric Power Research Institute, Jinan 250003, People's Republic of China

applications [7]. Actually, the Pt-free electrocatalysts like Pd have attracted attention for EOR in alkaline media because of their excellent electroactivity, rapid reaction kinetics, and the probability of using carbon material support to reduce the load of Pd nanoparticles (NPs) [9]. In our days, Pd NPs in catalysts are the most popular and extensive for EOR because they can exist increased surface area and considerable edges and corner atoms to improve the catalytic performance [10]. Meanwhile, Pd NPs can absorb more hydrogen than bulk Pd materials, which indicate the great electrochemical performance of Pd NPs [11, 12]. Therefore, these attractive properties of Pd-based electrocatalysts for ethanol oxidation provide the justification for the choice of the study. However, the efficiency and activity of Pd-based catalysts still have some restrictions for DEFCs, including that Pd NPs would aggregate and then lead to low catalytic activity because of the high surface energies [13]. To improve electrocatalytic activity and decrease the aggregation of Pd-based catalysts, many methods have been proposed in some literatures, such as making single metal into alloying catalysts [14], changing the morphologies of metal NPs [15], synthesizing composites based on different supporting materials [16]. Nickel foam (NF) also can be used as both an electrocatalyst in itself and as a Pt electrocatalyst support material for its open-pore structures, high specific surface areas, and good stability in a range of different electrolytes, including strongly alkaline conditions [17–19].

Graphene oxide (GO), as a two-dimensional nanosheet material, possesses excellent high conductivity, high specific surface area, and high carrier mobility and thermal stability [20, 21]. Simultaneously, GO also contains many oxygen-containing functional groups as nucleation centers which can provide abundant active sites for NPs and achieve distinguished functions in organic chemistry, electrochemistry, and nanotechnology [21, 22]. These excellent properties make GO become an outstanding and popular substitute to replace the conventional carbon support materials for wide application [20]. Additionally, the reduction of GO (rGO) was obtained by many methods, such as thermal, light, and chemical reduction [23].

Furthermore, the localized surface plasmon resonance (LSPR) effect is a significant factor to research the noble metal nanostructures and photochemistry [24]. At present, the metallic NPs upon LSPR excitation are applied in electrochemical reactions [25]. On the other hand, the LSPR effect of Pd NPs can be detected in ultraviolet-visible range [26]. Aasaithambi Kalaiselvi et al. described the apparent LSPR effect of Pd NPs with the absorbance within the peak range of 350 to 400 nm, and the optimized experiment time was observed [27]. And it also displayed the LSPR of Pd NPs with the absorbance 362 nm by V N Kalpana et al. [28].

In addition, polydopamine (PDA) acts as a suitable adhesive polymeric material that exhibits great conductivity and biocompatibility [29]. PDA was prepared by one-step self-polymerization in an aqueous solution of dopamine under weak alkaline conditions (pH = 8.5) [30]. The existence of functional group ($-NH_2$) in PDA causes electrochemically active nitrogen to be doped in the graphene to enhance their conductivity and reduce the accumulation of graphene [31].

In this paper, we presented a simple chemical method and annealing process to synthesize the composite material (Pd/rGO/PDA@NF) of Pd NPs, rGO, and PDA on nickel foam (NF) substrate for ethanol electrocatalysis. In our work, we used rGO as carbon support material to load Pd NPs. The GO was deposited on the NF by using PDA polymer film through a facile immersing method. The precursor K_2PdCl_4 was reduced to Pd NPs by ascorbic acid and the LSPR peak of NPs provided powerfully evidence to determine the concentration of precursor K_2PdCl_4 solution. The GO was reduced to rGO through annealing process while Pd NPs and substrate combined more inseparable. The poisoning resistance to carbonaceous intermediate species and catalytic oxidation activity of Pd/rGO/PDA@NF were researched. The stability of the electrocatalyst was also investigated by electrochemical workstation.

Experimental Sections

Materials and Reagents

Nickel foam (NF) was obtained from Kunshan Toll Hui Electronics Technology Co., Ltd. Quartz slice (QS) was obtained from Donghai Alfa Quartz products Co., Ltd. Potassium chloropalladite (K_2PdCl_4, 98%) and dopamine hydrochloride ($C_8H_{11}NO_2{\cdot}HCl$, 98%) were obtained from Aladdin Industrial Co., Ltd. Ethanol (C_2H_5OH, ≥ 99.7%), potassium hydroxide (KOH, ≥ 85.0%), hydrochloric acid (HCl, 36 ~ 38%), phosphoric acid (H_3PO_4, > 85%), sulfuric acid (H_2SO_4, 95% ~ 98%), and acetone (CH_3COCH_3, ≥ 95%) were obtained from Beijing Fine Chemical Co., Ltd. L-Ascorbic acid ($C_6H_8O_6$) was purchased from Sinopharm Chemical Reagent Co., Ltd. Purified water was utilized in all experiments. All of chemicals used in our work were analytical purity grade and without further purification.

Preparation of Samples

Synthesis of GO

The GO was synthesized from graphite by modified Hummers method [32]. A mixture acid with 9:1 volume ratio of 98% H_2SO_4 and 85% H_3PO_4 was added in the 250 mL three-necked flask with the mixture of graphite powder (0.75 g) and $KMnO_4$ solid (4.85 g) at ice-water bath. Then the reaction solution was heated and stirred in 50 °C for 12 h. Then reaction was cooled to room temperature. After that, the mixture

was poured and stirred into ice (100 g) with dropped 30% H_2O_2 (0.75 mL). The reaction product was centrifuged to obtain the precursor graphene oxide. The product was washed in succession with 30% HCl solution and with 5% HCl solution. For each wash, the mixture was centrifuged in 30 min and the supernatant decanted away. Finally, the product was filtered with a PVDF membrane to make the solution neutral with purified water. The solid obtained on the filter was dried at room temperature before use.

Synthesizing the Composite of Pd NPs, rGO, and PDA on QS (Pd/rGO/PDA@QS)

In order to analyze the relationship between LSPR peak and the concentration of precursor K_2PdCl_4 solution, the Pd/rGO/PDA@QS synthesized in different concentrations of K_2PdCl_4 solution were measured by UV-visible spectroscopy. At first, the QS slices (20 mm × 10 mm × 1 mm) were ultrasonically cleaned by purified water, acetone, ethanol, and purified water in proper order to dislodge impurities and then dried them at 60 °C. Subsequently, 0.5 mol L^{-1} NaOH solution was dropped into 20 mg mL^{-1} dopamine solution to adjust its pH to 8.5. The cleaned QS slices were immersed in the above-prepared dopamine solution for 2 h at room temperature and the PDA film was grown on the QS to obtain PDA@QS. Next, 0.5 mg mL^{-1} homogeneous GO suspension was obtained by ultrasonicated for 2.5 h. The sample of PDA@QS was put in the GO suspension at 60 °C for 3 h to obtain the GO/PDA@QS. Then GO/PDA@QS was immersed in precursor K_2PdCl_4 solution with the existence of ascorbic acid (0.1 mol L^{-1}) in water bath at 60 °C for 80 min to obtain Pd/GO/PDA@QS. In addition, the concentration of precursor K_2PdCl_4 solution was 1 mmol L^{-1}, 2 mmol L^{-1}, 3 mmol L^{-1}, 4 mmol L^{-1}, and 5 mmol L^{-1}, respectively. At last, the above Pd/GO/PDA@QS samples were annealed for 2 h at 200 °C to obtain the Pd/rGO/PDA@QS composites.

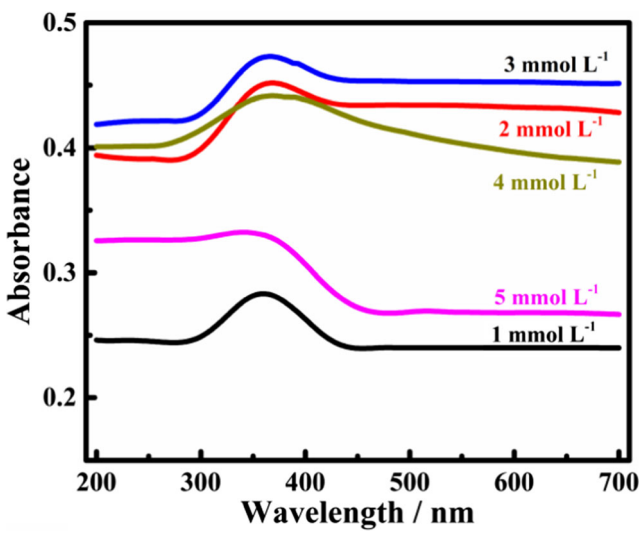

Fig. 1 The LSPR effect of the Pd/rGO/PDA@QS composites in different concentrations of K_2PdCl_4 solution. Lines 1, 2, 3, 4, and 5 corresponded to the spectra of Pd NPs in Pd/rGO/PDA@QS samples, which were obtained from different concentrations of K2PdCl4 solution, respectively, 1 mmol L^{-1}, 2 mmol L^{-1}, 3 mmol L^{-1}, 4 mmol L^{-1}, and 5 mmol L^{-1}

Synthesis of Pd/rGO/PDA@NF

Pd/rGO/PDA@NF was synthesized by the similar method to analyze the electrocatalytic performance and stability of this composite material. The concentration of K_2PdCl_4 solution is 3 mmol L^{-1} from LSPR effect of Pd NPs in Pd/rGO/PDA@QS composite. The NF sheets (20 mm × 10 mm × 1 mm) were ultrasonically cleaned by purified water, acetone, ethanol, and purified water in proper order to remove the impurities, then dried at 60 °C. Thereafter, the synthesis process of PDA film on the NF surface (PDA@NF) was same as the fabrication procedure of PDA@QS, only the QS substrate was changed to NF sheet. Then, the fabrication process of GO film on the surface of PDA@NF (GO/PDA@NF), Pd NPs on the surface of GO/PDA@NF composite (Pd/GO/PDA@NF), and Pd/rGO/PDA@NF were also the same as the synthesis procedure of GO/PDA@QS, Pd/GO/PDA@QS, and Pd/rGO/PDA@QS, respectively, only the quartz slices were replaced to the nickel foam sheets. In addition, the composite of Pd NPs, PDA, and NF (Pd/PDA@NF) was synthesized by the similar method of Pd/rGO/PDA@NF, but without adding GO.

Characterization

LSPR spectra were recorded by UV-visible (Hitachi U-3310) with the detection range of 200 ~ 700 nm. The morphologies and chemical elements of the as-prepared composites were obtained by scanning electron microscope (SEM, S-4800, Hitachi, Japan) with an energy dispersive spectrometer (EDS) analysis. The morphology and lattice structures of composites surface were further characterized by a high-resolution transmission electron microscope (TEM, JEM-2100, Japan). Raman spectra were carried out by using a Micro Confocal Laser Raman Spectrometer and the source of radiation was Ar^+ laser with wavelength of 514.5 nm. The structure and crystallization properties of the samples were characterized by the X-ray diffractometer (D8 ADVANCE, Bruker, Germany) with Cu K_α radiation ($\lambda = 0.1542$ nm) at 40 kV and 40 mA with a scan rate of 7°min^{-1}. X-ray photoelectron spectroscopy (XPS) measurements were performed by Model PHI 5300 (USA) to analyze the valence and state of chemical elements. The loading of Pd on the electrocatalyst surface was detected by inductively coupled plasma-optical emission spectrometry (ICP-OES, iCAP6300, ThermoFisher).

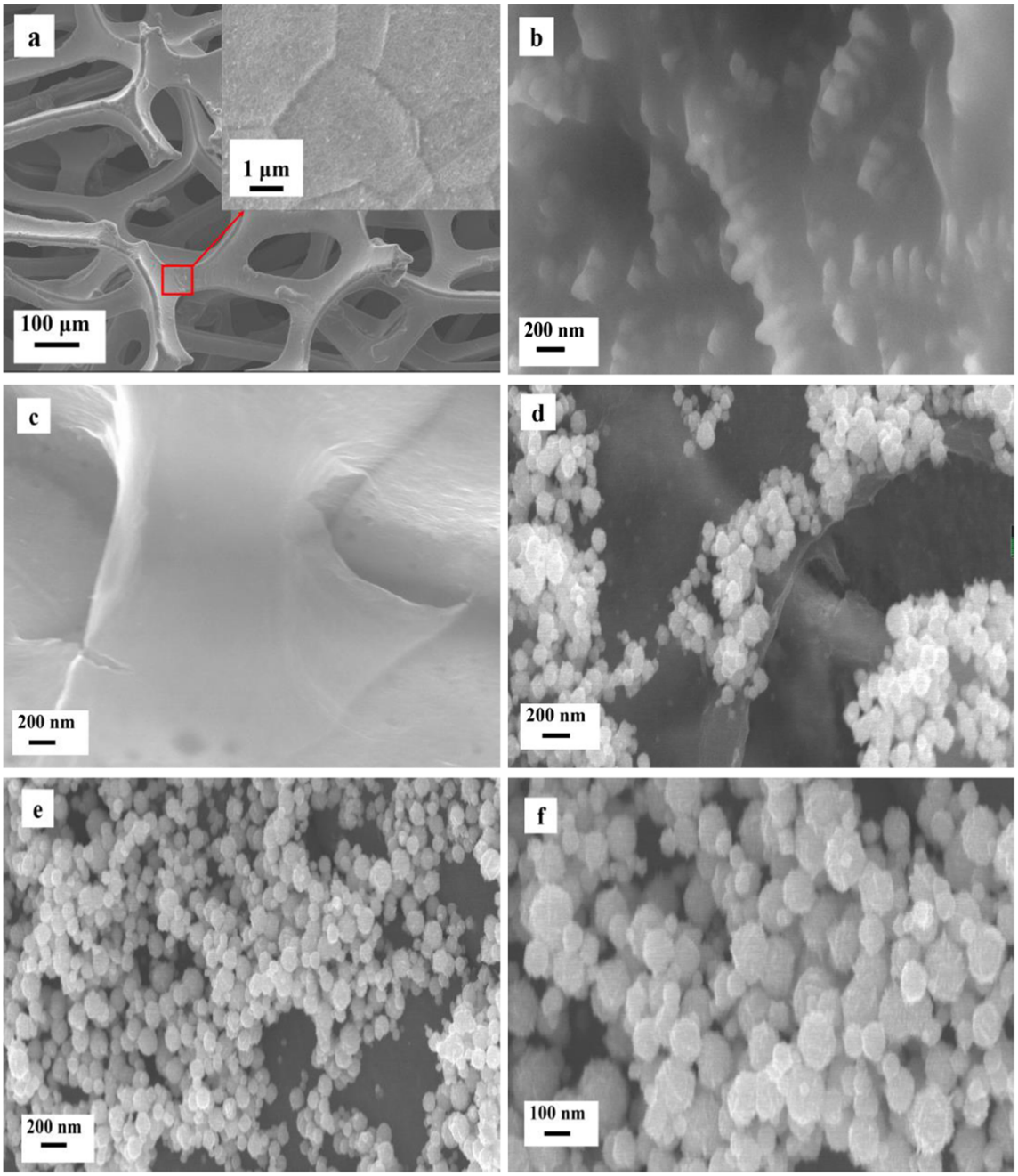

Fig. 2 SEM images of different composite surface: (**a**) NF, (**b**) PDA@NF, (**c**) GO/PDA@NF, (**d**) Pd/GO/PDA@NF, (**e**) and (**f**) Pd/rGO/PDA@NF

Electrochemical Measurements

The property of electrocatalyst was performed by the electrochemical workstation (CHI 760E, CH instruments, Shanghai) using a standard three electrodes in alkaline medium at room temperature. The counter electrode and reference electrode were platinum sheet (2.0 cm × 1.0 cm) and saturated calomel electrode (SCE), respectively. The as-prepared composites were used directly as working electrodes. The cycle voltammetry (CV) was measured by electrochemical workstation to assess the electrocatalytic performance of composites. The KOH solution was used as the electrolyte to provide conductive effect for ethanol electrochemical test. The potentially dissolved oxygen solution in electrolyte was removed by bubbling high purity N_2 for 15 min before electrochemical measurements. The range of voltage potential was limited from −0.8 to 0.3 V (vs. SCE) of the CV performance and any CV curves were activated after 40 cycles for stabilization.

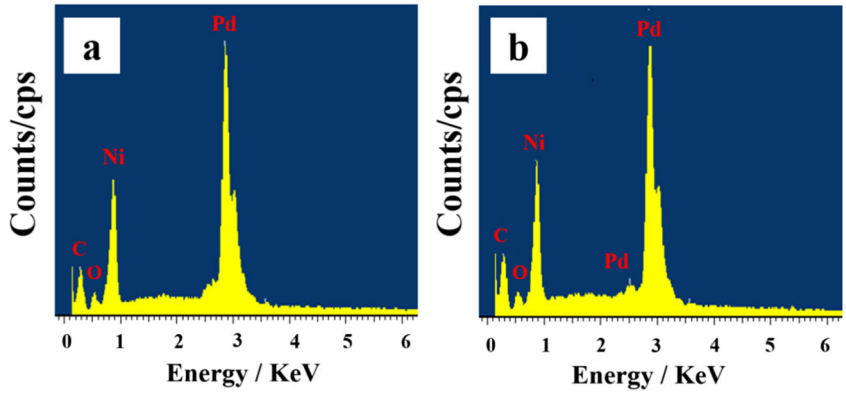

Fig. 3 EDS images of (**a**) Pd/GO/PDA@NF and (**b**) Pd/rGO/PDA@NF

Results and Discussion

The electrocatalyst was synthesized by a combined chemical and annealing method. The Pd NPs as an effective component of electrocatalyst were obtained by precursor K_2PdCl_4, which was reduced by ascorbic acid. The rGO could provide large surface area to load Pd NPs for enhancing electrochemical activity of ethanol oxidation. The morphology and chemical composition of the composite material can be characterized by SEM, EDS, TEM, XRD, Raman spectra, XPS, and ICP-OES. Moreover, the LSPR effect and electrochemical measurement determined the optimal experimental conditions and the electrocatalytic activity or stability for ethanol oxidation, respectively.

LSPR Effect

The Pd NPs exhibited distinct LSPR absorption peaks at the range of 300 ~ 800 nm due to different concentrations of precursor K_2PdCl_4 solution [33]. In order to select the optimal concentration of precursor K_2PdCl_4 solution, the LSPR absorption peaks of Pd/rGO/PDA@QS were carried out to determine the absorption peak of Pd NPs. As shown in Fig. 1, the intensity of absorbance increased as the concentration of the precursor K_2PdCl_4 solution up to 3 mmol L^{-1}, and then it gradually decreased with the concentration increasing to 5 mmol L^{-1}. This also indicated that the absorbance peaks of Pd NPs were in the range of 340 ~ 370 nm and the strongest LSPR peak was attributed by line 3, which was obtained from 3 mmol L^{-1} K_2PdCl_4 solution. Therefore, according to the LSPR effect of Pd NPs in the composites, the optimal concentration of K_2PdCl_4 solution was determined to be 3 mmol L^{-1}.

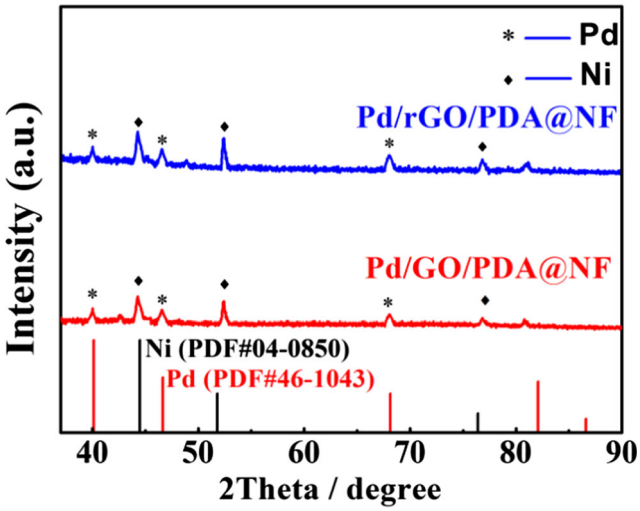

Fig. 4 XRD patterns of Pd/GO/PDA@NF and Pd/rGO/PDA@NF composites

Morphology and Composition Analysis

The synthesized composites were scanned by SEM to obtain the surface morphology. The SEM images of different composites were shown in Fig. 2, containing NF, PDA@NF, GO/PDA@NF, Pd/GO/PDA@NF, and Pd/rGO/PDA@NF. In Fig. 2a, the three-dimensional NF sheet showed the numerous and average networks in the frame structure which provided the huge supporting base for rGO or Pd NPs. After immersing in PDA solution, it can be obviously observed that the PDA particles were uniformly distributed on the NF surface as shown in Fig. 2b, which could provide a certain amount of adherence points for the adsorption of GO. This also confirmed that the PDA was successfully adsorbed on the NF surface. Then, by comparing with Fig. 2b, it can be clearly seen that the GO-like wavy tulle was successfully deposited on the PDA@NF surface as shown in Fig. 2c. Moreover, the wrinkled GO can reduce the contact resistance and preserve the porous structure to support active points [31].

As can be seen from Fig. 2(d–f), the similar shape of spherical Pd NPs were successfully grown on the GO/PDA@NF surface in Pd/GO/PDA@NF and Pd/rGO/PDA@NF. The numerous spherical Pd NPs were dispersed on the GO film with the similar diameter of 30 to 200 nm in two composites. Compared with two samples (Fig. 2d and 2e), it can be found that Pd NPs of Pd/rGO/PDA@NF (Fig. 2e) were grown more inseparable and combined with the substrate stronger than unannealed Pd NPs (Fig. 2d). And this phenomenon was more

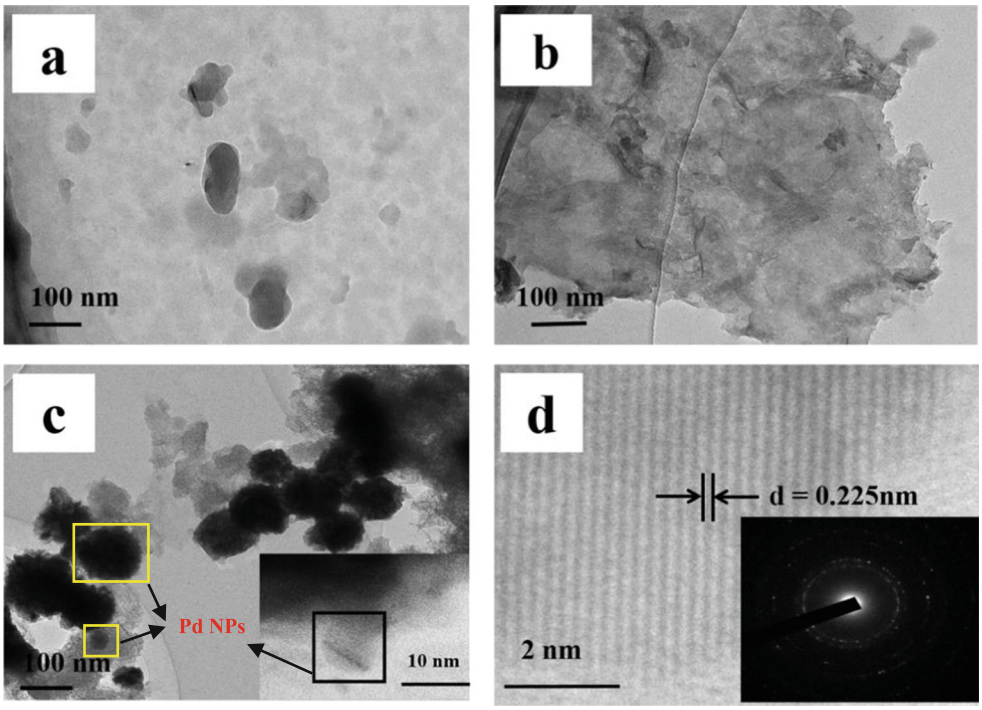

Fig. 5 TEM images of PDA (**a**), GO/PDA (**b**) and Pd/rGO/PDA (**c**), and HRTEM of Pd/rGO/PDA (**d**). The inset of **c** is the morphology of the small Pd NPs. The inset of (**d**) is the SAED patterns of Pd/rGO/PDA

pronounced at higher magnifications of Pd/rGO/PDA@NF in Fig. 2f.

The chemical components of the Pd/GO/PDA@NF and Pd/rGO/PDA@NF composites were also determined by EDS spectra as shown in Fig. 3. The EDS spectra of Pd/GO/PDA@NF and Pd/rGO/PDA@NF displayed the main dispersion of elements Pd and Ni on the surface, which confirmed that the Pd NPs were successfully deposited on the composite surface.

XRD measurement was carried out to further analyze the crystallization state and compositions of Pd/GO/PDA@NF and Pd/rGO/PDA@NF composites. As shown in Fig. 4, three diffraction peaks at 44.30°, 52.42°, and 76.80° were assigned to Ni(111), Ni(200), and Ni(220) lattice planes of cubic nickel

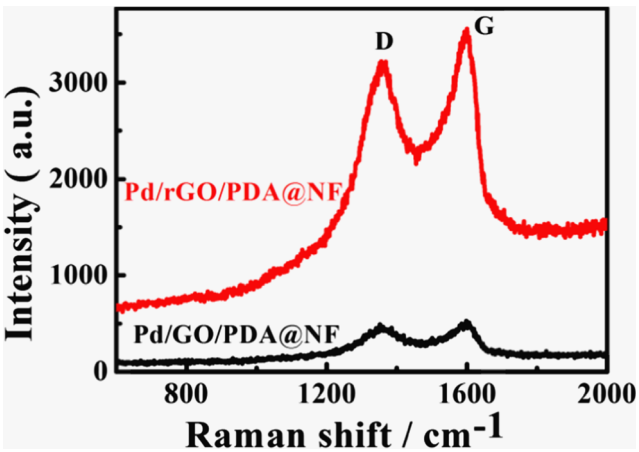

Fig. 6 Raman spectra of Pd/GO/PDA@NF and Pd/rGO/PDA@NF composites

(JCPDS 04-0850) in XRD curves of two composites. In addition, the standard diffraction peaks at $2\theta = 40.0°$, 46.6°, and 68.1° corresponded to the (111), (200), and (220) lattice planes of cubic palladium (JCPDS 46-1043), respectively. So the similar peaks at $2\theta = 40.1°$, 46.7°, and 68.1° in two curves of Fig. 4 were obtained, which corresponded well to the (111), (200), and (220) lattice planes of cubic Pd.

TEM analysis was measured to further investigate the surface morphology and crystal structural features of the composites in more detail by high-resolution transmission electron microscope (HRTEM) and selected area electronic diffraction (SAED). The TEM images in Fig. 5(a–c) displayed the morphologies of PDA, GO, and Pd NPs, consistent with SEM (Fig. 2) observations. Using the graphene as a support, large amounts of little spherical Pd NPs with a diameter of 8 nm aggregated into the relatively homogeneous spheres with average sizes of 100 nm. These homogeneous spheres were anchored onto the GO sheet, as shown in Fig. 5c and the inset. The lattice fringes in Fig. 5d were measured to be 0.225 nm, and according to the Bragg's Law $2d\sin\theta = n\lambda$, where d is the interplanar spacing of Pd NPs, θ is the diffraction angle between the incident X-ray and the corresponding crystal plane, n is the diffraction order ($n = 1$), and λ is the X-ray wavelength ($\lambda = 0.1542$ nm). So we can obtain the value $2\theta = 40.1°$, which can be assigned to cubic Pd (111) lattice planes. The SAED patterns (inset of Fig. 5d) contained several concentric diffraction rings of spots, suggesting that the spherical Pd NPs are polycrystalline state. In addition, the lattice fringe of Pd NPs was calculated from SAED patterns as 0.225 nm, confirming the presence of cubic phase Pd(111) lattice planes.

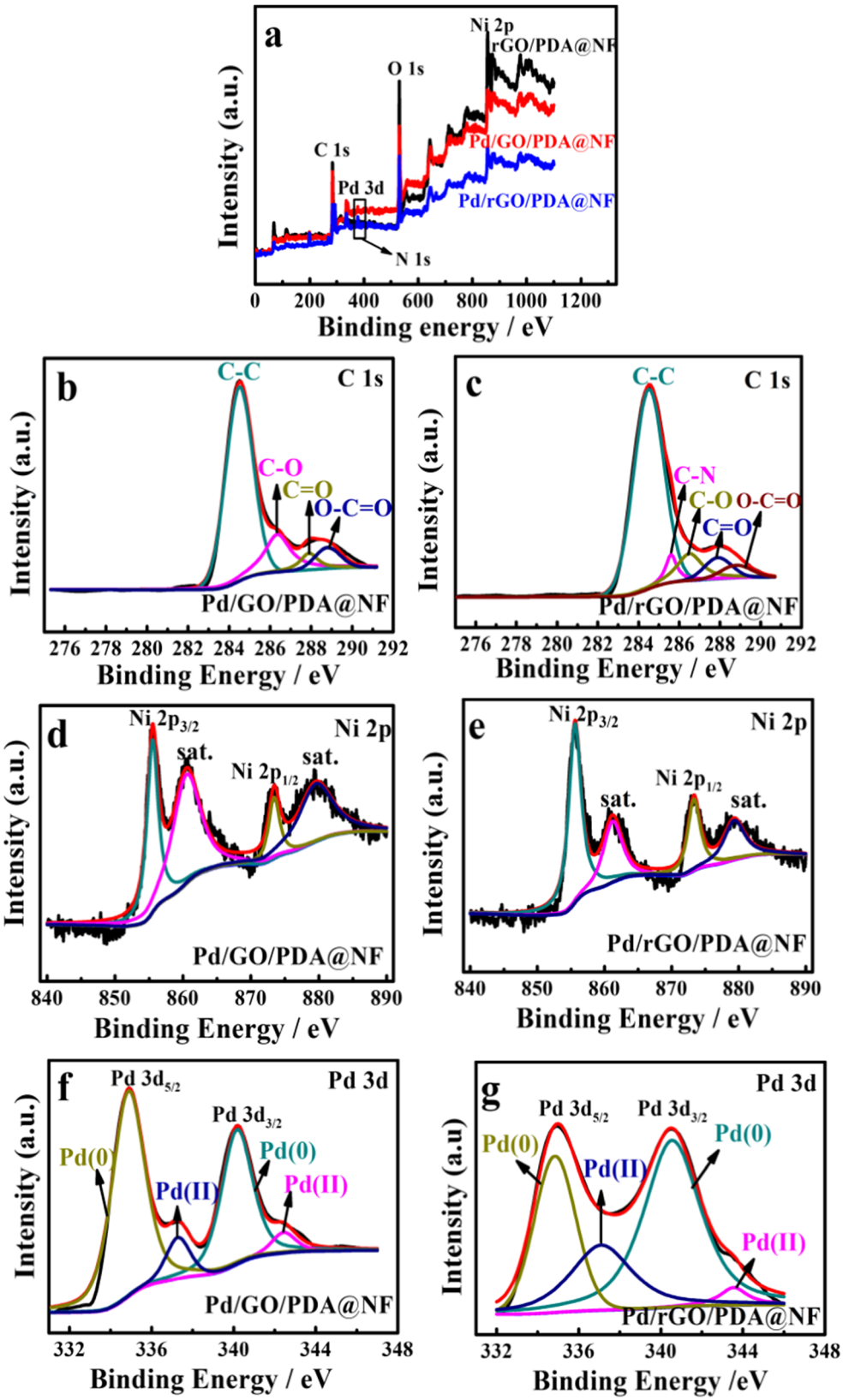

Fig. 7 **(a)** XPS full scan spectrum of different composites: rGO/PDA@NF, Pd/GO/PDA@NF, Pd/rGO/PDA@NF; (**b**) C 1s XPS core level spectra of Pd/GO/PDA@NF composite; (**c**) C 1s XPS core level spectra of Pd/rGO/PDA@NF composite; (**d**) Ni 2p XPS core level spectra of Pd/GO/PDA@NF composite; (**e**) Ni 2p XPS core level spectra of Pd/rGO/PDA@NF composite; (**f**) Pd 3d XPS survey spectra of Pd/GO/PDA@NF; (**g**) Pd 3d XPS survey spectra of Pd/rGO/PDA@NF

Raman spectra have become a widely used method to analyze and characterize the structural, double carbon-carbon bonds, and electron-phonon coupling in graphene [34, 35]. The peak at about 1600 cm^{-1} is G peak which results from

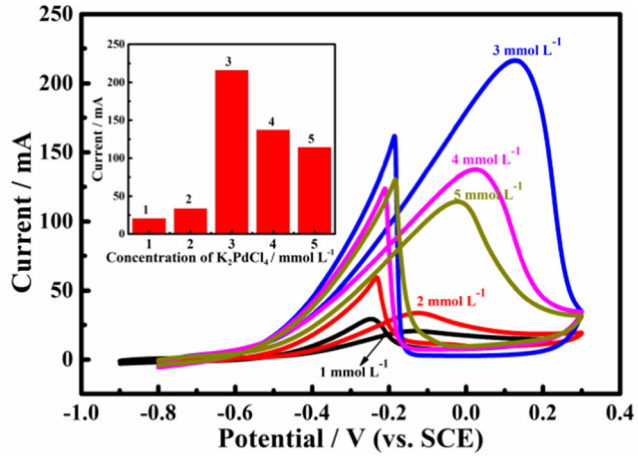

Fig. 8 The CV curves of Pd/rGO/PDA@NF in different concentrations of K_2PdCl_4 solution: 1 mmol L^{-1}, 2 mmol L^{-1}, 3 mmol L^{-1}, 4 mmol L^{-1}, 5 mmol L^{-1}. The inset is a plot of current density and concentration of K_2PdCl_4

first-order scattering of the E_{2g} mode for sp^2 carbon atoms [36]; while the other is D peak at around 1350 cm^{-1} which comes from the structural defects or grain boundaries of amorphous carbon species [36]. Therefore, the Raman spectra of Pd/GO/PDA@NF and Pd/rGO/PDA@NF composites were measured to prove that the GO was reduced to rGO after annealing. As can be seen in Fig. 6, the two characteristic peaks of Pd/GO/PDA@NF and Pd/rGO/PDA@NF composites corresponding to G peak and D peak at around 1600 cm^{-1} and 1351 cm^{-1} were obtained, respectively. Generally, the intensity ratio (I_D/I_G) between D peak and G peak is associated with the density of defects and graphitization for graphene-based materials [37]. So we draw the conclusion in Fig. 6, the I_D/I_G ratio of Pd/GO/PDA@NF (0.93) was higher than Pd/rGO/PDA@NF (0.89), indicating that the defects of GO were more than rGO. This confirmed that the GO had been reduced to rGO after annealed for high temperature.

Furthermore, the XPS measurement can give assistance to analyze compositions and structure to further supplement the information of the composites. The XPS spectra were used to characterize the composites to further confirm the chemical states of specific ingredients and demonstrate particle surface character of the composites. The XPS full scan spectrum of rGO/PDA@NF, Pd/GO/PDA@NF, and Pd/rGO/PDA@NF was determined in Fig. 7a, which mainly displayed the carbon, oxygen, nitrogen, palladium, and nickel species. For three composites, the peak located at 284 eV and 530 eV was ascribed to the characteristic peak of C 1 s and O 1 s, respectively. The peak located at 400 eV was attributed to the characteristic peak of N 1 s, which showed that the PDA was successfully coated on the surface of NF sheet of all composites. In addition, the Pd 3d peak at about 338 eV was observed in the spectrum of Pd/GO/PDA@NF and Pd/rGO/PDA@NF by comparison in three composites, indicating that Pd NPs were deposited on the GO/PDA@NF surface.

In detail, as can be seen from the Fig. 7b, the C 1s spectrum of Pd/GO/PDA@NF can be split into four peaks with binding energies at about 284.5 eV, 286.4 eV, 287.9 eV, and 288.8 eV, corresponding to C-C, C-O, C=O, and O-C=O species, respectively [38, 39]. In Fig. 7c, the C 1s XPS spectrum of Pd/rGO/PDA@NF can be divided to five peaks with binding energies at about 284.5 eV, 285.6 eV, 286.4 eV, 287.9 eV, and288.8 eV, which related to C-C, C-N, C-O, C=O, and O-C=O species. By comparing Figs. 7b and c, it can be obviously shown that the existence of C-N bond at binding energy 285.6 eV citified the presence of PDA on the surface of nickel foam in Pd/rGO/PDA@NF and demonstrated a little amount of N element from PDA layer was doped in the rGO.

The XPS spectrum of Ni 2p peak in Fig. 7d and e indicated the chemical states of the nickel substrate. In Fig. 7d, the two main peaks of binding energy of Ni $2p_{3/2}$ and Ni $2p_{1/2}$ at 855.7 eV and 873.3 eV with two satellite peaks, respectively, which revealed the oxidation state of Ni^{2+} [40]. Compared with Fig. 7e, the height of satellite peak of Ni $2p_{3/2}$ and Ni $2p_{1/2}$ were smaller than their own, the intensity of Ni 2p peak in the surface of Pd/rGO/PDA@NF significantly decreased due to being annealed at high temperature. Annealing can eliminate the internal stress, reduce the high hardness, and enhance the interactions of Pd NPs, GO, PDA, and NF. The main difference between images Fig. 7d and e of Pd/GO/PDA@NF and Pd/rGO/PDA@NF is also from the annealed process. The XPS spectrum of Pd 3d peak for Pd/GO/

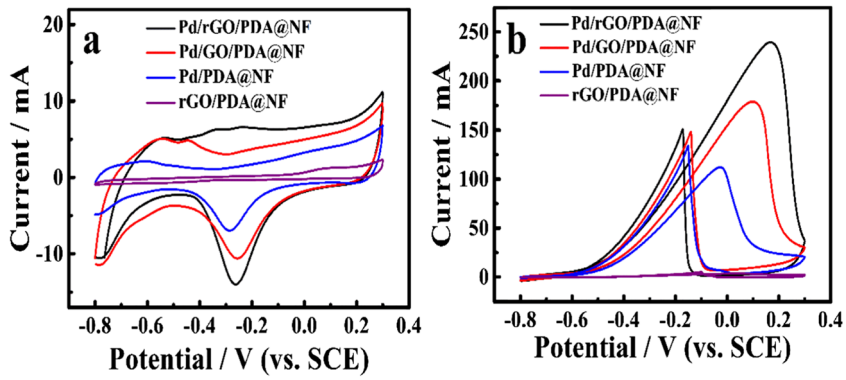

Fig. 9 The CV curves of Pd/rGO/PDA@NF, Pd/GO/PDA@NF, Pd/PDA@NF and rGO/PDA@NF in (a) 1 mol L^{-1} KOH solution; (b) 1 mol L^{-1} KOH electrolyte containing 1 mol L^{-1} ethanol at 100 mV s^{-1}

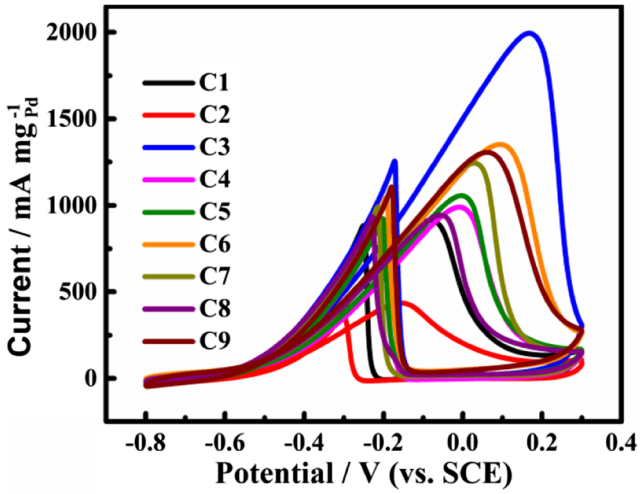

Fig. 10 The CV curves of Pd/rGO/PDA@NF synthesized by different conditions C1, C2, C3, C4, C5, C6, C7, C8, and C9 in the solution containing 1 mol L^{-1} KOH and 1 mol L^{-1} ethanol at 100 mV s^{-1}, respectively

PDA@NF in Fig. 7f presented two main peaks of binding energy at 335.0 eV (Pd $3d_{5/2}$) and 340.1 eV (Pd $3d_{3/2}$), respectively, which displayed the presence of Pd (0) [41] and the weaker couple of 336.9 eV (Pd $3d_{5/2}$) and 342.4 eV (Pd $3d_{3/2}$) corresponded to Pd (II) [41]. In comparison with Fig. 7f, the Pd 3d binding energies of Pd/rGO/PDA@NF were slightly shifted for higher values than Pd/GO/PDA@NF composite. The shift of binding energies of Pd 3d core level could modify the electronic structure and reflect the change of d-band center relative Fermi level [42, 43].

Electrochemical Performance of As-prepared Electrodes

The crucial factors in assessing performance of electrocatalyst include tolerance to the carbonaceous species and catalytic activity. The cycle voltammetry (CV) was measured to determine the electrochemical properties of those electrocatalysts or electrodes.

Figure 8 presented CV curves of Pd/rGO/PDA@NF fabricated in different concentrations of K_2PdCl_4 solution. The fabrication of Pd/rGO/PDA@NF composite in 3 mmol L^{-1} K_2PdCl_4 solution exhibited the maximum current value. And the inset of Fig. 8 showed the significant relationship between current and concentration of K_2PdCl_4 solution. The best electrocatalytic performance in EOR was consistent with the strongest LSPR effect. So Pd/rGO/PDA@NF fabricated in 3 mmol L^{-1} K_2PdCl_4 solution was selected to determine the electrochemical behavior in EOR.

Table 1 The I_f/I_b of Pd/rGO/PDA@NF synthesized by different operation conditions

Samples	C1	C2	C3	C4	C5	C6	C7	C8	C9
I_f/I_b	1.04	1.22	1.59	1.07	1.15	1.29	1.26	1.01	1.19

Figure 9a showed the CV curves of Pd/rGO/PDA@NF, Pd/GO/PDA@NF, Pd/PDA@NF, and rGO/PDA@NF in the potential range of −0.8 to 0.3 V (vs. SCE) at a scan rate of 100 mV s^{-1} in 1 mol L^{-1} KOH solution. The CV profile of rGO/PDA@NF is essentially featureless in the potential range of −0.8 to 0.3 V, which may be caused by interference from the PDA and graphene [18]. The CV curves of Pd/rGO/PDA@NF, Pd/GO/PDA@NF, and Pd/PDA@NF displayed the similar appearance with the reduction peak of PdO at the potential range of −0.3 to −0.2 V (vs. SCE). Another CV curve of rGO/PDA@NF showed the gentle trend and not contained the reduction peak of PdO. As shown in Fig. 9b, the CV curves of Pd/rGO/PDA@NF, Pd/GO/PDA@NF, Pd/PDA@NF, and rGO/PDA@NF electrodes in the solution containing 1 mol L^{-1} KOH and 1 mol L^{-1} ethanol at a scan rate of 100 mV s^{-1} were observed. Two oxidation peaks different from Fig. 9a can be obviously depicted in Pd/rGO/PDA@NF, Pd/GO/PDA@NF, and Pd/PDA@NF, which confirmed the electrocatalytic activity of these as-prepared composites in a solution of 1 mol L^{-1} KOH and 1 mol L^{-1} ethanol. However, the ethanol oxidation peak of rGO/PDA@NF in the electrolyte was hardly observed, indicating the absence of electrochemical activity. In addition, the peak current intensity of Pd/rGO/PDA@NF was higher than Pd/GO/PDA@NF and Pd/PDA@NF obviously, which displayed the better electrocatalytic performance of Pd/rGO/PDA@NF for ethanol oxidation. The presence of rGO can enhance the electrochemical activity toward ethanol electrocatalysis by comparing Pd/rGO/PDA@NF and Pd/PDA@NF.

The reverse scan peak of CV curves in EOR is related to the intermediates of ethanol and these reaction intermediates will result in low activity of catalyst, which can be named "catalyst poisoning" [41]. Generally, a ratio of forward scan peak current intensity (I_f) to reverse scan peak current intensity (I_b) for CV curves can evaluate the tolerance limit and catalytic activity of the catalysts to intermediate carbonaceous species [42, 44]. To select the optimal experimental conditions for the excellent ethanol electrocatalytic performance, the orthogonal test of four factors at three different levels was carried out in Table S1 (Supplementary material).

We synthesized Pd/rGO/PDA@NF composites in nine conditions and named them C1, C2, C3, C4, C5, C6, C7, C8, and C9.

The CV curves of Pd/rGO/PDA@NF for different conditions were measured in the aqueous solution of 1 mol L^{-1} KOH and 1 mol L^{-1} ethanol at 100 mV s^{-1} as shown in Fig. 10. There are two apparent oxidation peaks: one peak at −0.1 to 0.15 V appears during forward scan and comes from

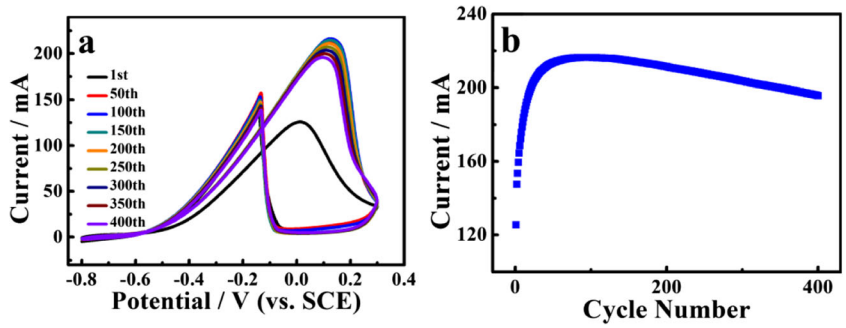

Fig. 11 (**a**) The CV curves of Pd/rGO/PDA@NF from the first to the 400th cycle in the solution of 1 mol L^{-1} KOH and 1 mol L^{-1} ethanol at a scan rate of 100 mV s^{-1}; (**b**) The current intensity of forward scan peak vs. cycle number plot. Pd/rGO/PDA@NF was synthesized by C3 in Table S1

ethanol oxidation peak; the other peak at − 0.25 to − 0.15 V occurs in reverse scan and results from the oxidation reaction of carbonaceous species. Additionally, the values of I_f/I_b were summarized in Table 1. The Pd/rGO/PDA@NF ($I_f/I_b = 1.59$) was synthesized by C3 in Table S1, which was higher than others. This result indicated that Pd/rGO/PDA@NF synthesized in C3 has excellent tolerance to carbonaceous intermediates and higher ethanol catalytic performance than others. So, we next selected C3 to synthesize Pd/rGO/PDA@NF for all of ethanol oxidation tests. In addition, the electrochemical active surface area (ECSA) of electrocatalysts is other important parameter to evaluate the electrochemical activity. The ECSA was calculated by this equation: [45]

$$ECSA = \frac{Q}{m \times C} \tag{1}$$

where Q is the charge associated with the reduction of PdO on the surface (mC), m is the mass of metallic Pd (mg), and C is the reduction charge density for PdO monolayer (0.405 mC/cm^2). The ECSA of Pd/rGO/PDA@NF was calculated to be 19.08 m^2 g^{-1} by this equation.

The poisoning effect against carbonaceous intermediates is associated to the ethoxi species (CH_3CO_{ads}) and the hydroxyl species (OH_{ads}) on the catalyst surface in electrolyte. The possible mechanism between CH_3CO_{ads} and OH_{ads} on Pd-based electrocatalyst toward ethanol oxidation can be depicted as following steps [46, 47]:

$$Pd + OH^- \rightleftharpoons Pd{-}OH_{ads} + e^- \tag{2}$$

$$Pd + CH_3CH_2OH \rightleftharpoons Pd{-}(CH_3CH_2OH)_{ads} \tag{3}$$

$$Pd{-}(CH_3CH_2OH)_{ads} + 3OH^{-1} \rightarrow Pd{-}(CH_3CO)_{ads} + 3H_2O + 3e^- \tag{4}$$

$$Pd{-}(CH_3CO)_{ads} + Pd{-}OH_{ads} \rightarrow Pd{-}CH_3COOH + Pd \tag{5}$$

$$Pd{-}CH_3COOH + OH^{-1} \rightarrow Pd + CH_3COO^- + H_2O \tag{6}$$

Meanwhile, the electrocatalytic stability of catalysts was an important evaluation standard for ethanol oxidation. The stability of catalyst toward ethanol oxidation was measured by the CV curves with multiple cycles. As shown in Fig. 11a, the CV curves of Pd/rGO/PDA@NF displayed a trend that the current intensity of forward and reverse scan peaks increased gradually before the 100th cycle and then declined after achieving the highest value of the current intensity. In detail, the current intensity of positive and negative scan peaks at the first cycle increased from 125.7 mA and 146.9 mA to 216.2 mA and 153.3 mA in the 100th cycle. This is indicative of overall increase of the current intensity of Pd most likely via increase of active surface areas of rGO from the first – 100th cycle [17]. Then the current intensity at both forward and reverse scan peaks gradually reduced from the 100th to the 400th and they were observed 195.7 mA and 138.7 mA in the 400th cycle. This is indicative of overall loss of the current intensity of Pd most likely via detachment and electrodissolution of Pt particles and poisoning to carbonaceous intermediates species from the 100th to the 400th cycle [18]. In addition, the value of peak potential increased in the cycle process. The reason of shift in peak potential may be the

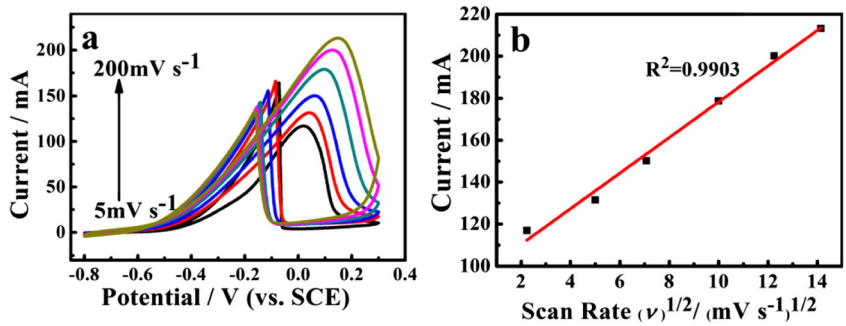

Fig. 12 (**a**) The CV curves of Pd/rGO/PDA@NF in the solution of 1 mol L^{-1} KOH and 1 mol L^{-1} ethanol at different scan rates of 5 mV s^{-1}, 25 mV s^{-1}, 50 mV s^{-1}, 100 mV s^{-1}, 150 mV s^{-1}, and 200 mV s^{-1}. (**b**) The graph of current intensity vs. square roots of scan rate. Pd/rGO/PDA@NF was synthesized by C3 in Table S1

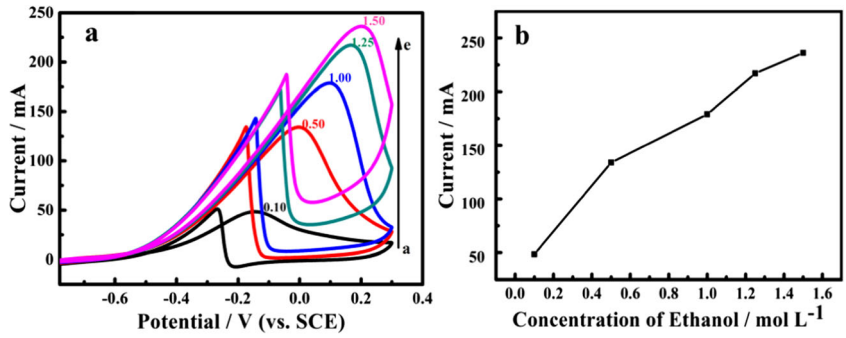

Fig. 13 (**a**) CV plots of Pd/rGO/PDA@NF in the solution of 1 mol L^{-1} KOH and different concentrations of ethanol (**a**–**e**): 0.10, 0.50, 1.00, 1.25, and 1.50 mol L^{-1}; (**b**) the plot of current intensity vs. concentration of ethanol solution. Pd/rGO/PDA@NF was synthesized by C3 in Table S1

continuous production of carbon intermediates during the reaction.

As shown in Fig. 11b, the stability of Pd/rGO/PDA@NF was performed by current intensity of forward scan peak vs. cycle number to evaluate the long-term cycle stability directly of this catalyst toward ethanol oxidation. More evidently, the current intensity of forward scan peak gradually increased from the first cycle, then achieved the top point (216.2 mA). Next, the current intensity showed a slow decline in the cyclic process which meant the decreasing of the electrocatalytic performance for Pd/rGO/PDA@NF. It was found that the current intensity remained a stable decrease trend and kept 90.6% of the maximum value after 400 cycles. During the cyclic process, it showed that Pd/rGO/PDA@NF possessed a superior long-term stability.

The CV curves of Pd/rGO/PDA@NF toward ethanol oxidation in 1 mol L^{-1} KOH solution containing 1 mol L^{-1} ethanol solution at different scan rates were shown in Fig. 12a. Evidently, the current intensity of forward and reverse scan peaks increased with the addition of scan rates in the same electrolyte. So Pd/rGO/PDA@NF exhibited great electrocatalytic performance with the increasing of scan rates for ethanol oxidation. As shown in Fig. 12b, the relationship between the current intensity of forward scan peak and square roots of scan rate was obviously linear ($R^2 = 0.9903$). This indicated that the ethanol electrocatalysis on Pd/rGO/PDA@NF was a diffusion-controlled process.

The concentration of ethanol or KOH solution also affects the catalytic activity toward ethanol oxidation. The current intensity of forward and reverse scan peak can change gradually with the variable concentration of the electrolyte.

The CV curves were measured in existence of different concentrations of ethanol (a–e) with 1 mol L^{-1} KOH solution at scan rate of 100 mV s^{-1} in Fig. 13a. The current intensity of forward and reverse scan peaks gradually raised with the increase of ethanol concentration. Furthermore, the current intensity added obviously with an increase of ethanol concentration in Fig. 13b, which clearly displayed the excellent electrocatalytic performance for ethanol catalytic oxidation with the increasing of ethanol concentration.

The Fig. 14a showed the CV curves in the solution of 1 mol L^{-1} ethanol and different concentrations of KOH (a–e) at a scan rate of 100 mV s^{-1}. The current intensity of forward and reverse scan peaks increased with addition of KOH concentration. Figure 14b obviously showed the increasing trend of current intensity with different concentrations of KOH solution. Additionally, the Pd/rGO/PDA@NF did not have obvious catalytic activity when the concentration of KOH solution was 0.10 mol L^{-1}. So KOH electrolyte provides conductive effect in ethanol eletrocatalytic oxidation [40]. The catalytic activity of Pd/rGO/PDA@NF enhanced during frequent potential cycling change in the electrolyte with higher concentrations of KOH or ethanol in Figs. 13 and 14.

The catalytic parameters of Pd/rGO/PDA@NF catalyst and the electrochemical measurement results obtained from previously reported literatures are compared in Table 2, including the comparison of the peak potential, I_f/I_b and ECSA of catalysts containing Pd NPs or rGO. In

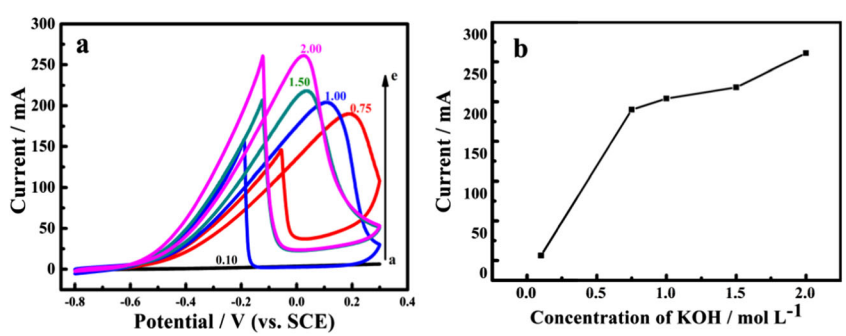

Fig. 14 (**a**) CV curves of Pd/rGO/PDA@NF in the solution of 1 mol L^{-1} ethanol and different concentrations of KOH (**a**–**e**): 0.10, 0.75, 1.00, 1.50, and 2.00 mol L^{-1}; (**b**) the plot of current intensity vs. concentration of KOH solution. Pd/rGO/PDA@NF was synthesized by C3 in Table S1

Table 2 Summary of literature catalytic parameters in ethanol oxidation of various Pd-based electrocatalysts

Electrode	Peak potential (V)	I_f/I_b	ECSA (m^2 g^{-1})	Reference
Pd/RGO/GC	− 0.28[a] (vs. SCE)	0.90[a]	21.80	[16]
Pd@CoP NSs/CFC	−0.25[a](vs. SCE)	1.04[a]	40.30	[45]
Pt-Pd(1:3)/RGO/GC	− 0.29[a] (vs. SCE)	1.17[a]	–	[48]
Pd/GN/GC	− 0.27[a] (vs. SCE)	1.08[a]	24.6	[49]
Pd/rGO/PDA@NF	0.1 (vs. SCE)	1.59	19.08	This work

[a] The value was evaluated from CV curves in the literatures

this table, Pd/rGO/PDA@NF holds a higher value of I_f/I_b and similar ECSA value. The excellent performance of Pd/rGO/PDA@NF for ethanol oxidation can attribute to NF, rGO, and Pd NPs. Firstly, NF can provide the large surface area for substance deposited. Secondly, the rGO can supply large surface area and good conductivity. Layered rGO existed abundant active sites to support more Pd NPs. The Pd NPs will be dispersed uniformly on the surface of rGO, and reduced the agglomeration of Pd NPs. The good electrical conductivity of rGO and the excellent activity of Pd can be able to act synergistically together in ethanol electrocatalysis. At last, Pd NPs exhibited great electrocatalytic performance of anti-poisoning to carbonaceous intermediates and stability toward ethanol catalytic test.

Conclusions

The composite material of Pd nanoparticles, graphene, and polydopamine based on three-dimensional nickel foam substrate was successfully synthesized for ethanol oxidation. Pd nanoparticles were obtained via reduction of precursor K_2PdCl_4 using ascorbic acid at 60 °C for 80 min. Localized surface plasmon resonance was performed to determine the optimal synthesized condition by absorbance peak to obtain Pd nanoparticles. The nickel foam substrate provided a considerable support structure, which brought a large surface area for supporting polydopamine, graphene, and Pd nanoparticles. Moreover, polydopamine as a binder combined nickel foam with graphene closer. The Pd nanoparticles acted as an effective ingredient of electrocatalyst and graphene existed large surface area and could supply large amounts of active sites for nanoparticles toward ethanol oxidation. The higher ratio of forward scan to reverse scan peak current intensity ($I_f/I_b = 1.59$) was observed through the analysis of electrochemical test, suggesting that the composite material exhibited a higher tolerance of against poisoning to carbonaceous intermediate species and excellent catalytic activity. In addition, the peak current intensity of forward scan peak retained 90.6% of maximum value after 400 cycles, which powerfully demonstrated the great stability of the composite material. The excellent electrocatalyst can be obtained by this synthesized method, which could be used as a promising electrochemical catalyst material toward ethanol oxidation for fuel cell.

Funding Information We gratefully acknowledge the National Natural Science Foundation of China (No. 21271027) for their support of this work.

References

1. Y. Oh, J. Kang, S. Nam, S. Byun, B. Park, Pt/$AlPO_4$ nanocomposite thin-film electrodes for ethanol electrooxidation. Mater. Chem. Phys. **135**(1), 188–192 (2012)
2. J. Yin, S. Shan, M.S. Ng, L. Yang, D. Mott, W. Fang, N. Kang, J. Luo, C.J. Zhong, Catalytic and electrocatalytic oxidation of ethanol over palladium-based nanoalloy catalysts. Langmuir **29**(29), 9249–9258 (2013)
3. Y. Zhang, Q. Yi, H. Chu, H. Nie, Catalytic activity of Pd-Ag nanoparticles supported on carbon nanotubes for the electro-oxidation of ethanol and propanol. J. Fuel Chem. Technol. **45**(4), 475–483 (2017)
4. Y. Tao, A. Dandapat, L. Chen, Y. Huang, Y. Sasson, Z. Lin, J. Zhang, L. Guo, T. Chen, Pd-on-Au supra-nanostructures decorated graphene oxide: an advanced electrocatalyst for fuel cell application. Langmuir **32**(34), 8557–8564 (2016)
5. M. Liu, Y. Lu, W. Chen, PdAg nanorings supported on graphene nanosheets: highly methanol-tolerant cathode electrocatalyst for alkaline fuel cells. Adv. Funct. Mater. **23**(10), 1289–1296 (2013)

6. A.A. El-Shafei, A.M. Abd Elhafeez, H.A. Mostafa, Ethanol oxidation at metal–zeolite-modified electrodes in alkaline medium. Part 2: palladium–zeolite-modified graphite electrode. J. Solid State Electrochem. **14**(2), 185–190 (2009)
7. Z. Zhang, L. Xin, K. Sun, W. Li, Pd–Ni electrocatalysts for efficient ethanol oxidation reaction in alkaline electrolyte. Int. J. Hydrog. Energy **36**(20), 12686–12697 (2011)
8. C.W. Xu, H. Wang, P.K. Shen, S.P. Jiang, Highly ordered Pd nanowire arrays as effective electrocatalysts for ethanol oxidation in direct alcohol fuel cells. Adv. Mater. **19**(23), 4256–4259 (2007)
9. A.K. Ipadeola, R. Barik, S.C. Ray, K.I. Ozoemena, Bimetallic Pd/SnO_2 nanoparticles on metal organic framework (MOF)-derived carbon as electrocatalysts for ethanol oxidation. Electrocatalysis **10**(4), 366–380 (2019)
10. X. Chen, G. Wu, J. Chen, X. Chen, Z. Xie, X. Wang, Synthesis of "clean" and well-dispersive Pd nanoparticles with excellent electrocatalytic property on graphene oxide. J. Am. Chem. Soc. **133**(11), 3693–3695 (2011)
11. A. Zalineeva, S. Baranton, C. Coutanceau, G. Jerkiewicz, Electrochemical behavior of unsupported shaped palladium nanoparticles. Langmuir **31**(5), 1605–1609 (2015)
12. A. Zalineeva, S. Baranton, C. Coutanceau, G. Jerkiewicz, Octahedral palladium nanoparticles as excellent hosts for electrochemically adsorbed and absorbed hydrogen. Sci. Adv. **3**(2), 1–10 (2017)
13. M. Gopiraman, D. Deng, K. Zhang, W. Kai, I. Chung, R. Karvembu, I.S. Kim, Utilization of human hair as a synergistic support for Ag, Au, Cu, Ni, and Ru nanoparticles: application in catalysis. Ind. Eng. Chem. Res. **56**(8), 1926–1939 (2017)
14. C. Kung, P. Lin, Y. Xue, R. Akolkar, L. Dai, X. Yu, C. Liu, Three dimensional graphene foam supported platinum–ruthenium bimetallic nanocatalysts for direct methanol and direct ethanol fuel cell applications. J. Power Sources **256**, 329–335 (2014)
15. M. Li, P. Liu, R.R. Adzic, Platinum monolayer electrocatalysts for anodic oxidation of alcohols. J. Phys. Chem. Lett. **3**(23), 3480–3485 (2012)
16. Q. Zhang, L. Jiang, H. Wang, J. Liu, J. Zhang, Y. Zheng, F. Li, C. Yao, S. Hou, Hollow graphitized carbon nanocage supported Pd catalyst with excellent electrocatalytic activity for ethanol oxidation. ACS Sustain. Chem. Eng. **6**(6), 7507–7514 (2018)
17. J. van Drunen, B. Kinkead, M.C. Wang, E. Sourty, B.D. Gates, G. Jerkiewicz, Comprehensive structural, surface-chemical and electrochemical characterization of nickel-based metallic foams. ACS Appl. Mater. Interfaces **5**(14), 6712–6722 (2013)
18. J. van Drunen, B.K. Pilapil, Y. Makonnen, D. Beauchemin, B.D. Gates, G. Jerkiewicz, Electrochemically active nickel foams as support materials for nanoscopic platinum electrocatalysts. ACS Appl. Mater. Interfaces **6**(15), 12046–12061 (2014)
19. M. Grden, M. Alsabet, G. Jerkiewicz, Surface science and electrochemical analysis of nickel foams. ACS Appl. Mater. Interfaces **4**(6), 3012–3021 (2012)
20. B. Men, Y. Sun, Y. Tang, L. Zhang, Y. Chen, P. Wan, J. Pan, Highly dispersed Ag-functionalized graphene electrocatalyst for oxygen reduction reaction in energy-saving electrolysis of sodium carbonate. Ind. Eng. Chem. Res. **54**(30), 7415–7422 (2015)
21. C. Wang, D. Astruc, Recent developments of metallic nanoparticle-graphene nanocatalysts. Prog. Mater. Sci. **94**, 306–383 (2018)
22. Y. Li, Y. Zhang, F. Li, M. Li, L. Chen, Y. Dong, Q. Wei, Sandwich-type amperometric immunosensor using functionalized magnetic graphene loaded gold and silver core-shell nanocomposites for the detection of carcinoembryonic antigen. J. Electroanal. Chem. **795**, 1–9 (2017)
23. L. Zhang, T. Wu, X. Xu, F. Xia, H. Na, Y. Liu, H. Qiu, W. Wang, J. Gao, Magnetic bimetallic nanoparticles supported reduced graphene oxide nanocomposite: fabrication, characterization and catalytic capability. J. Alloys Compd. **628**, 364–371 (2015)
24. K.M. Mayer, J.H. Hafner, Localized surface plasmon resonance sensors. Chem. Rev. **111**(6), 3828–3857 (2011)
25. C. Wang, X.G. Nie, Y. Shi, Y. Zhou, J.J. Xu, X.H. Xia, H.Y. Chen, Direct plasmon-accelerated electrochemical reaction on gold nanoparticles. ACS Nano **11**(6), 5897–5905 (2017)
26. C. Xu, F. Qin, Q. Zhu, J. Lu, Y. Wang, J. Li, Y. Lin, Q. Cui, Z. Shi, A.G. Manohari, Plasmon-enhanced ZnO whispering-gallery mode lasing. Nano Res. **11**(6), 3050–3064 (2018)
27. A. Kalaiselvi, S.M. Roopan, G. Madhumitha, C. Ramalingam, G. Elango, Synthesis and characterization of palladium nanoparticles using *Catharanthus roseus* leaf extract and its application in the photo-catalytic degradation. Spectrochim. Acta, Part A **135**, 116–119 (2015)
28. V.N. Kalpana, V.D. Rajeswari, Synthesis of palladium nanoparticles via a green route using *Lagenaria siceraria*: assessment of their innate antidandruff, insecticidal and degradation activities. Mater. Res. Express **5**(11), 115406 (2018)
29. J. Feng, P. Zhang, A. Wang, Q. Liao, J. Xi, J. Chen, One-step synthesis of monodisperse polydopamine-coated silver core–shell nanostructures for enhanced photocatalysis. New J. Chem. **36**(1), 148–154 (2012)
30. H. Lee, S.M. Dellatore, W.M. Miller, P.B. Messersmith, Mussel-inspired surface chemistry for multifunctional coatings. Science **318**(5849), 426–430 (2007)
31. G. Liu, S. Lu, W. Xu, G. He, Y. Zheng, Y. Cheng, Fabrication of graphene/copper–nickel foam composite for high performance supercapacitors. New J. Chem. **42**(12), 9455–9462 (2018)
32. D.C. Marcano, D.V. Kosynkin, J.M. Berlin, A. Sinitskii, Z. Sun, A. Slesarev, L.B. Alemany, W. Lu, J.M. Tour, Improved synthesis of graphene oxide. ACS Nano **4**(8), 4806–4814 (2010)
33. D.S. Sheny, D. Philip, J. Mathew, Rapid green synthesis of palladium nanoparticles using the dried leaf of *Anacardium occidentale*. Spectrochim. Acta Part A **91**, 35–38 (2012)
34. S. Sahoo, G. Khurana, S.K. Barik, S. Dussan, D. Barrionuevo, R.S. Katiyar, In situ raman studies of electrically reduced graphene oxide and its field-emission properties. J. Phys. Chem. C **117**(10), 5485–5491 (2013)
35. K.N. Kudin, B. Ozbas, H.C. Schniepp, R.K. Prud'homme, I.A. Aksay, R. Car, Raman spectra of graphite oxide and functionalized graphene sheets. Nano Lett. **8**(1), 36–41 (2008)
36. B. He, Z. Ren, S. Yan, Z. Wang, Large area uniformly oriented multilayer graphene with high transparency and conducting properties derived from highly oriented polyethylene films. J. Mater. Chem. C **2**(30), 6048–6055 (2014)
37. J. Balamurugan, T.D. Thanh, S. Heo, N.H. Kim, J.H. Lee, Novel route to synthesis of N-doped graphene/Cu–Ni oxide composite for high electrochemical performance. Carbon **94**, 962–970 (2015)
38. Y. Zhang, M. Park, H.Y. Kim, B. Ding, S.-J. Park, In-situ synthesis of nanofibers with various ratios of $BiOCl_x/BiOBr_y/BiOI_z$ for effective trichloroethylene photocatalytic degradation. Appl. Surf. Sci. **384**, 192–199 (2016)
39. Y. Zheng, S. Lu, W. Xu, G. He, Y. Cheng, T. Yu, Y. Zhang, The fabrication of graphene/polydopamine/nickel foam composite material with excellent electrochemical performance as supercapacitor electrode. J. Solid State Chem. **258**, 401–409 (2018)
40. Y. Cheng, M. Guo, Y. Yu, M. Zhai, R. Guo, J. Hu, Fabrication of coral-like Pd based porous MnO_2 nanosheet arrays on nickel foam for methanol electrooxidation. Ind. Eng. Chem. Res. **57**(32), 10893–10904 (2018)
41. S. Fu, C. Zhu, D. Du, Y. Lin, Facile one-step synthesis of three-dimensional Pd-Ag bimetallic alloy networks and their electrocatalytic activity toward ethanol oxidation. ACS Appl. Mater. Interfaces **7**(25), 13842–13848 (2015)
42. G. Ren, Y. Liu, W. Wang, M. Wang, Z. Zhang, Y. Liang, S. Wu, J. Shen, Facile synthesis of highly active three-dimensional urchin-like Pd@PtNi nanostructures for improved methanol and ethanol

electrochemical oxidation. ACS Appl. Nano Mater. **1**(7), 3226–3235 (2018)

43. P. Wu, H. Zhang, Y. Qian, Y. Hu, H. Zhang, C. Cai, Composition- and aspect-ratio-dependent electrocatalytic performances of one-dimensional aligned Pt–Ni nanostructures. J. Phys. Chem. C **117**(37), 19091–19100 (2013)
44. E. Wu, Q. Zhang, A. Xie, W. Yang, C. Peng, J. Hou, Y. He, B. Zhang, L. Deng, Synthesis of hollow echinus-like Au@PdAgNSs decorated reduced graphene oxide as an excellent electrocatalyst for enhanced ethanol electrooxidation. J. Alloys Compd. **789**, 174–182 (2019)
45. S. Ye, J. Feng, G. Li, Pd nanoparticle/CoP nanosheet hybrids: highly electroactive and durable catalysts for ethanol electrooxidation. ACS Catal. **6**(11), 7962–7969 (2016)
46. Z.X. Liang, T.S. Zhao, J.B. Xu, L.D. Zhu, Mechanism study of the ethanol oxidation reaction on palladium in alkaline media. Electrochim. Acta **54**(8), 2203–2208 (2009)
47. Z.R. Yang, S.Q. Wang, J. Wang, A.J. Zhou, C.W. Xu, Pd supported on carbon containing nickel, nitrogen and sulfur for ethanol electrooxidation. Sci. Rep. **7**(1), 15479 (2017)
48. F. Ren, H. Wang, C. Zhai, M. Zhu, R. Yue, Y. Du, P. Yang, J. Xu, W. Lu, Clean method for the synthesis of reduced graphene oxide-supported PtPd alloys with high electrocatalytic activity for ethanol oxidation in alkaline medium. ACS Appl. Mater. Interfaces **6**(5), 3607–3614 (2014)
49. J. Yang, Y. Xie, R. Wang, B. Jiang, C. Tian, G. Mu, J. Yin, B. Wang, H. Fu, Synergistic effect of tungsten carbide and palladium on graphene for promoted ethanol electrooxidation. ACS Appl. Mater. Interfaces **5**(14), 6571–6579 (2013)